

Simple, Fast, Accurate Melanocytic Lesion Segmentation in 1D Colour Space

F. Peruch¹, F. Bogo¹, M. Bonazza¹, M. Bressan¹, V. Cappelleri² and E. Peserico¹

¹*Dip. Ing. Informazione, Univ. Padova, Padova, Italy*

²*Dip. Medicina, Univ. Padova, Padova, Italy*

Keywords: Segmentation, Dermatoscopy, Melanoma, Melanocytic Lesion, Naevus.

Abstract: We present a novel technique for melanocytic lesion segmentation, based on one-dimensional Principal Component Analysis (PCA) in colour space. Our technique is simple and extremely fast, segmenting high-resolution images in a fraction of a second even with the modest computational resources available on a cell phone – an improvement of an order of magnitude or more over state-of-the-art techniques. Our technique is also extremely accurate: very experienced dermatologists disagree with its segmentations less than they disagree with the segmentations of all state-of-the-art techniques we tested, and in fact less than they disagree with the segmentations of dermatologists of moderate experience.

1 INTRODUCTION

Malignant melanoma is an aggressive form of skin cancer whose incidence is steadily growing worldwide (Rigel et al., 1996). Early diagnosis promptly followed by excision is crucial for patient survival. Unfortunately, in its early stages malignant melanoma appears very similar to a benign melanocytic lesion (a common mole). However, malignant melanoma can often be recognized even in its early stages by a trained dermatologist, particularly when observed through a *dermatoscope* – an instrument providing magnification and specific illumination.

The first step in the visual analysis of a melanocytic lesion is segmentation, i.e. classification of all points in the image as part of the lesion or of the surrounding, healthy skin. While segmentation is typically studied in the context of automated image analysis, it is a first, necessary step even for human operators who plan to evaluate quantitative features of a lesion such as diameter or asymmetry – e.g. in the context of epidemiological studies correlating those features to lesion benignity (Stolz et al., 1994).

The most important aspect of a segmentation technique is accuracy. Accuracy is usually evaluated in terms of divergence from the segmentation provided by one or more human “experts”. The most widely used metric is simply the number of misclassified pixels normalized over the size of the lesion (Joel et al., 2002). A crucial observation is that even expert der-

matologists differ in their assessment of a lesion’s border (see Figure 1), since lesions are often fuzzy and there exists no standard operative definition of whether a portion of skin belongs to a lesion or not – dermatologists rely on subjective judgement developed over years of dermatoscopic training. The area of the disagreement region is typically 10 – 20% of the area of the lesion itself (Silletti et al., 2009; Belloni Fortina et al., 2011); this is obviously the minimum divergence that an automated system can be expected to have when evaluated against human experts.

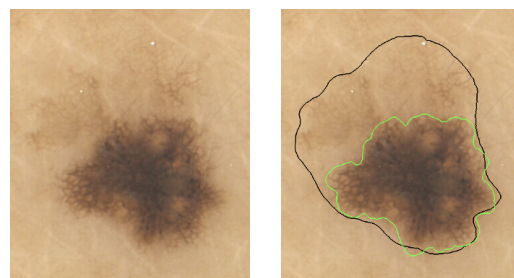


Figure 1: A dermatoscopically imaged melanocytic lesion (left) and two widely divergent segmentations obtained from two experienced dermatologists (right).

The second crucial aspect of an automated segmentation technique is its computational efficiency. A slow segmentation slows down any system based on it, meaning such a system cannot be used by a dermatologist performing real-time diagnosis. This

is particularly important for hand-held, portable systems operating with limited computational resources.

This work presents a novel technique for the automated segmentation of dermatoscopically imaged melanocytic lesions. Our technique is extremely accurate: very experienced dermatologists disagree with its results less than they disagree with those of dermatologists of moderate experience. It is also extremely fast, segmenting high-resolution images in a fraction of a second even with the modest computational resources available on a cell phone – an order of magnitude faster than the fastest techniques in the literature.

The rest of this work is organized as follows. Section 2 provides a brief review of the state of the art on melanocytic lesion segmentation. Section 3 introduces our novel approach, based on one-dimensional Principal Component Analysis (PCA) of the colour space of the image. Section 4 presents an experimental comparison of our technique with other segmentation approaches, in terms of accuracy and computational efficiency. Finally, Section 5 summarizes our results and discusses their significance.

2 RELATED WORK

Numerous methods have been proposed for lesion segmentation in dermatoscopic images. According to a classification commonly adopted in image segmentation (Szeliski, 2010), we can separate them into three main classes.

The first class aims at identifying lesion boundaries by use of edges and smoothness constraints. A good representative of this class is GVF Snakes (Erkol et al., 2005). The accuracy in border identification may strongly depend on an initial segmentation estimate, on effective preprocessing (e.g. for hair removal) and on morphological postprocessing (Celebi et al., 2009; Silveira et al., 2009).

The second class includes “split and merge” techniques. These approaches proceed either by recursively splitting the whole image into pieces based on region statistics or, conversely, merging pixels and regions together in a hierarchical fashion. Representatives of this class include Modified JSEG (Celebi et al., 2007), Stabilized Inverse Diffusion Equations (SIDE) (Gao et al., 1998), Statistical Region Merging (SRM) (Celebi et al., 2008), Watershed (Wang et al., 2010). These algorithms are very sensitive to correct tuning of a large number of parameters, leading to highly variable performance (Gao et al., 1998; Silletti et al., 2009).

The third class of segmentation techniques for melanocytic lesions discriminates between lesion and

healthy skin on the image’s colour histogram. After a preprocessing phase, these approaches classify each *colour* as healthy skin or lesional tissue. This separation is mapped back onto the original image, from which morphological postprocessing then eliminates small, spurious “patches”. Representatives of this class include Mean-shift (Melli et al., 2006) and Fuzzy c-means (Schmid, 1999; Cucchiara et al., 2002; Silletti et al., 2009). Our approach belongs to this third class.

3 A FIVE-STAGE TECHNIQUE

Our technique proceeds in five stages.

The first stage (Subsection 3.1) is optional and simply preprocesses the image with an automated hair removal software. The second stage (Subsection 3.2) performs a Principal Component Analysis (PCA) of the colour histogram and reduces the dimensionality of the colour space to 1. The third stage (Subsection 3.3) applies a blur filter to the image projected on the 1D space, in order to reduce noise. The fourth stage (Subsection 3.4) separates the pixels into two clusters, segmenting the image into regions corresponding to lesional and healthy skin. The fifth and final stage (Subsection 3.5) morphologically postprocesses the image to remove spurious “patches” and to identify lesional areas of clinical interest.

3.1 Preprocessing

The presence of hair represents a common obstacle in dermatoscopic analysis of melanocytic lesions. Although our approach is relatively resilient to the presence of hair (see Section 4), in some cases automated hair removal significantly improves the final result. Thus, when necessary, we perform automated hair removal with VirtualShave (Fiorese et al., 2011).

3.2 PCA in Colour Space

PCA (Abdi and Williams, 2010) is a standard mathematical tool for statistical analysis of observations in a multi-dimensional space.

We employ PCA to cluster the colours of the image into two classes according to their projection on the first principal component of the colour histogram (where each point in the RGB space has a “mass” equal to the number of pixels with that colour). Using only one dimension runs against the common wisdom of melanocytic lesion segmentation through PCA: all work in this area suggested one should use not only

the first, but also the second principal component of the colour histogram.

In practice, we perform PCA on an m -pixel RGB image in four steps. First, we compute the mean R, G and B values of the image – the barycentre of the colour histogram. Then, we compute the 3×3 autocorrelation matrix $\mathbf{C} = \mathbf{M}^T \mathbf{M}$, where the i^{th} row $\mathbf{m}_i = \langle r_i g_i b_i \rangle$ of the $m \times 3$ matrix \mathbf{M} represents the three colour components of the i^{th} pixel, each component normalized by subtracting the mean value of that colour in the image. Effectively we have:

$$\mathbf{C} = \sum_i \mathbf{m}_i^T \mathbf{m}_i \quad (1)$$

so that \mathbf{C} can be easily computed by “streaming” the image pixel by pixel, subtracting the mean R, G, and B values, computing the 6 distinct products of the pixel’s colour components, and adding each of those products to the corresponding product for all other pixels (note that \mathbf{C} is characterized by 6 elements rather than 9 since it is symmetrical).

Then, we compute the eigenvectors of \mathbf{C} and take the dominant one, i.e. the first principal component of \mathbf{M} . This takes a negligible amount of time since it only requires computing the roots of a 3^{rd} degree polynomial (the characteristic polynomial of \mathbf{C}) and inverting a 3×3 matrix.

Finally, we project each row of \mathbf{M} onto the principal component obtaining a one channel grayscale image. Again, this can be achieved by “streaming” the image and performing only a few arithmetic operations for each pixel. Thus, the cost of the whole procedure is essentially that of scanning the image from main memory three times (once for the average, once for the covariance, once for the projection).

We noticed an extreme similarity between the dominant eigenvectors of different melanocytic lesion images. In a set of 60 images of different lesions from different patients, for any pair of dominant eigenvectors \mathbf{v} and \mathbf{u} , we found $|\mathbf{v} \cdot \mathbf{u}| > 0.99$.

We then decided to experiment with a simplified version of our technique, where instead of computing all eigenvectors of each image, one simply takes the (precomputed) average of the first eigenvector of a small “training set” of images. Throughout the rest of the article, we refer to this simplified version as *static* 1D-PCA. Section 4 shows that this crude approximation still yields surprisingly good results and, by completely bypassing the PCA portion of the computation, allows significant speedups.

Static 1D-PCA has another important advantage. Since the 1D colour space on which the image is projected is independent of the image, one could utilize the simplified technique with (cheaper) grayscale image acquisition equipment paired with an appropri-

ately tuned (physical) colour filter. This could allow considerable cost savings when developing biomedical equipment to e.g. evaluate size, growth patterns or asymmetry of melanocytic lesions.

3.3 Noise Reduction

In order to reduce noise, we blur the grayscale image corresponding to the projection on the first principal component. More precisely, we replace the value of each pixel with the average colour in the 11×11 pixel square surrounding it. This filter provides results comparable to those of a Gaussian filter, but is far more computationally efficient, requiring a single scan of the image and no floating point operations.

3.4 Colour Clustering

Operating on the colour histogram $h(\cdot)$ that associates to each colour c the number of pixels $h(c)$ of that colour, we separate colours (and thus pixels) into two clusters corresponding respectively to healthy skin and lesional tissue. This stage can be divided into a preprocessing phase and two main phases.

The preprocessing applies to the histogram a square root operator, followed by a moving average operator over a window of 11 points. More precisely, we have:

$$h'(x) = \sqrt{h(x)} \quad h''(x) = \frac{1}{11} \sum_{y=x-5}^{x+5} h'(y) \quad (2)$$

The square root operator enhances smaller values, which is useful when the percentages of healthy skin and lesional tissue differ widely. The averaging smooths out small fluctuations.

The second phase clusters colours in two steps. First we find the positions M_ℓ, M_s of two local maxima in $h''(\cdot)$ that can be assumed as “centres” of, respectively, the lesion cluster and the healthy skin cluster. Then, we determine a frontier point $F \in [M_\ell, M_s]$ separating the two clusters in the histogram.

The position M_1 of the first cluster centre corresponds to the position of the global maximum in $h''(\cdot)$ (see Figure 2). This cluster cannot be classified as lesion or healthy skin until the second centre position is found: lesion area may be larger or smaller than healthy skin area. The second cluster centre M_2 is computed as:

$$M_2 = \arg \max_x (h''(x)(h''(M_1) - h''(m_x))), x \neq M_1 \quad (3)$$

where $h''(m_x)$ is the minimum of $h''(\cdot)$ between x and M_1 . The two terms in the product being maximized ($h''(x)$ and $h''(M_1) - h''(m_x)$) are meant to

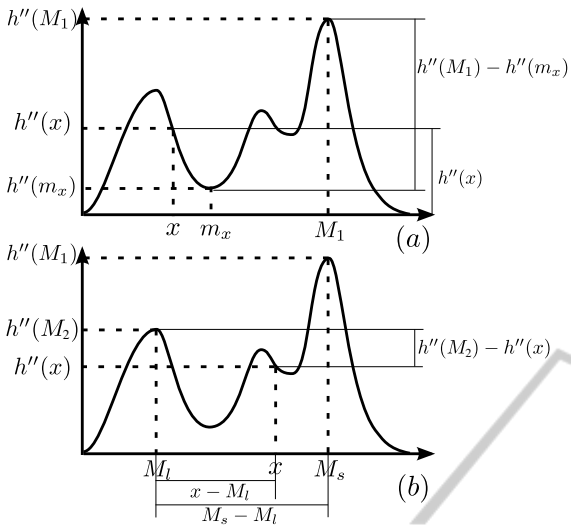


Figure 2: Identification of clusters centres M_ℓ and M_s in the colour histogram.

favour, in the choice of M_2 , a colour that is “well-represented” (yielding a high $h''(x)$) and at the same time is “sharply separated” from M_1 (yielding a high $h''(M_1) - h''(m_x)$). Remembering that lesional skin is darker than healthy skin, M_ℓ and M_s are then:

$$M_\ell = \min(M_1, M_2), M_s = \max(M_1, M_2) \quad (4)$$

Finally, we choose the separation point between skin colour and lesion colour as:

$$F = \arg \max_x \left(h''(M_2) - h''(x) \right) \left(\frac{x - M_\ell}{M_s - M_\ell} \right)^\gamma \quad (5)$$

where $\gamma \in \mathbb{R}^+$ is the single “tuning” parameter of our technique – the smaller γ , the “tighter” the segmentations produced. Informally, the first term in the product favours, as a separation point, a colour that is *not* well-represented and that thus yields a sharp separation between the two clusters. The second term, whose weight grows with γ , favours a colour closer to that of healthy skin; this attempts to reproduce the behaviour of human dermatologists, who tend to classify as lesion regions of the image that are slightly darker than the majority of the healthy skin, even when those regions are considerably lighter than the “core” of the lesion. Figure 3 illustrates how the clustering results vary as γ increases from 0.8 to 1. On our dataset, we obtained good results for all values of γ in $[1, 1.4]$. Note that the fractional exponentiation in equation 5 is carried out at most once for each of the 256 points of the colour histogram, incurring an overall computational cost that is virtually negligible (see Section 4).

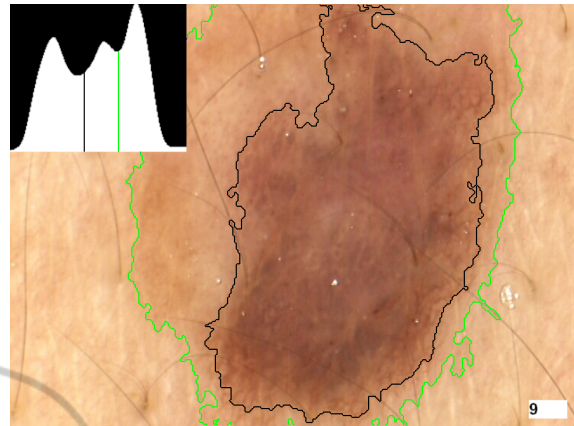


Figure 3: Identification of the separation point between skin colour and lesion colour for $\gamma = 1$ (green) and $\gamma = 0.8$ (black). Higher values of γ favour colours closer to that of healthy skin.

3.5 Postprocessing

Mapping the segmentation from colour space back onto the original image produces a binary mask, where each pixel is classified as lesional or healthy. The postprocessing stage makes this classification more accurate. First, it corrects several local artefact “patches” due to a pixel in the image being slightly darker or lighter than its neighbours. Second, it identifies all the connected components that, although classified as healthy, are entirely surrounded by lesional pixels; these components usually correspond to large air bubbles or regressions in a pigmented lesion, and should therefore be classified as lesional.

Our postprocessing involves two phases (see Figure 4). We first “downsample” the image in order to easily identify the *boundaries* of each lesional component through a simplified (and faster!) version of the technique described in (Suzuki et al., 2003). Then, we remove all boundaries delimiting connected components that are “too small”. We now describe each phase in greater detail.

Denote by p_{ij} the pixel located at row i and column j in an image, and by $v(p_{ij})$ its value. For any pixel, we consider its 4-way and 8-way *neighbourhood* – informally, the 4 pixels adjacent to it horizontally or vertically, and the 8 pixels adjacent to it horizontally, vertically or diagonally. More formally, for each *internal* (i.e. non-edge and non-corner) pixel p_{ij} of an image:

Definition 1. The 4-way neighbourhood of p_{ij} consists of the 4 pixels p_{kl} such that $|i - k| + |l - j| = 1$.

Definition 2. The 8-way neighbourhood of p_{ij} consists of the 8 pixels $p_{kl} \neq p_{ij}$ such that $|i - k| \leq 1$ and $|l - j| \leq 1$.

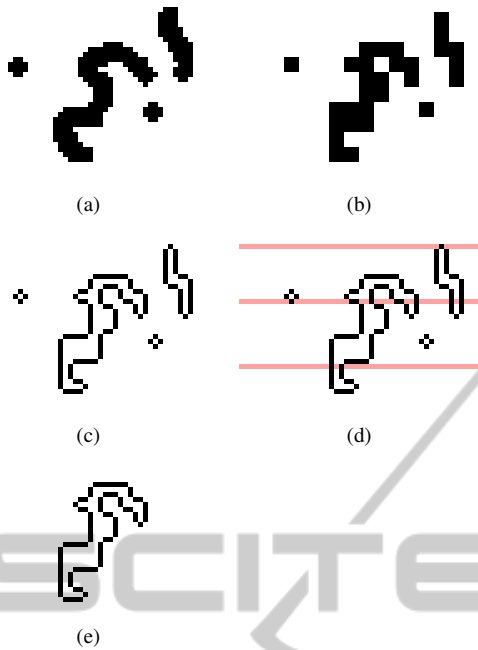


Figure 4: The postprocessing stage. (a) Initial binary mask. (b) Binary mask after downsampling. (c) Boundary pixels. (d) D -rows. (e) Single boundary encircling “sufficient” area.

We deal with pixels on the edges or corners of the image by surrounding the image with a 1-pixel-wide strip of *non-lesional* pixels so that the pixels of the original image correspond to the internal pixels of the expanded image.

In the downsampling phase, we partition the (expanded) image into boxes of 3×3 pixels; each pixel in a box takes the value of the central pixel in the box:

$$v(p_{ij}) \triangleq v(p_{kl}) \text{ with } k = 3 \left\lfloor \frac{i}{3} \right\rfloor + 1, l = 3 \left\lfloor \frac{j}{3} \right\rfloor + 1 \quad (6)$$

Then, we identify the *boundary* pixels in the image:

Definition 3. A *boundary pixel* is a *lesional pixel* whose 4-way neighbourhood contains exactly 3 *lesional pixels*.

It would be tedious but straightforward to verify that, due to the downsampling phase, the 8-way neighbourhood of any boundary pixel contains exactly 2 boundary pixels.

If we consider any boundary pixel as a vertex of degree 2 connected by an edge to its two adjacent boundary pixels, then we obtain a set of disjoint cycle graphs in the image, corresponding to the actual boundaries of all (putative lesional) connected components. This makes it extremely easy to “walk” a boundary, starting from any of its pixels, following the edges between adjacent vertices. Note that, up

to this stage, no explicit label has been assigned to any pixel since those satisfying the boundary definition are simply marked as “boundary pixels” without any distinction between different contours; this is the crucial simplification of our scheme compared to that of (Suzuki et al., 2003).

In the second step, we compute the area of all connected components of “sufficient” height – we can expect a minimum height for any lesion of clinical interest of 5% of the image’s height. More formally:

Definition 4. Consider an image of r rows, numbered from 1 to r starting from the top, and a parameter d ($1 \leq d \leq r$). We say the i^{th} row is a d -row if $i \bmod d = 0$.

Only boundary pixels belonging to a d -row serve as “starting points” to follow the corresponding boundary. From the boundary, we can easily obtain the area of the connected component, as follows. Let b_i be the i^{th} boundary pixel of the connected component on a generic row; then the pixels of the connected component in that row are those between any two consecutive boundary pixels b_i and b_{i+1} with i odd.

Every component with height at least d is “caught” by our technique, while smaller components *may be* missed (if no d -row intersects them) – but these “small” components are of no interest to us. d -rows allow considerable speedups as long as d is larger than 5 – 10; while d values equal to (or smaller than) 5% of the image’s height catch all lesions of clinical interest. Thus, we set d as 5% of the image’s height.

In the last step, all boundaries delimiting areas smaller than one fifth that of the largest connected component are removed. This takes care of both small dark patches in healthy skin, and small light patches within a lesion.

Note that, even if there are many known techniques to identify connected components in a binary image (Chang et al., 2004; Park et al., 2000; Martin-Herrero, 2007), they are not suitable for our purposes. Classic techniques (Chang et al., 2004; Park et al., 2000) are in general computationally expensive, requiring at least two scans of the image and/or the introduction of additional data structures; in contrast, our technique requires a single sequential pass plus a small number of additional accesses to a limited number of image pixels. Even the optimized, single-pass approach of (Martin-Herrero, 2007) requires approximately 30% more time than ours; and requires additional effort to “match” portions of the lesion or of the skin that do not belong to the same connected component.

4 EXPERIMENTAL EVALUATION

We evaluated our segmentation technique by comparing it to three different state-of-the-art techniques. After briefly describing our experimental setup (Subsection 4.1), we present the evaluation results in terms of both accuracy (Subsection 4.2) and computational efficiency (Subsection 4.3).

4.1 Experimental Setup

60 images of melanocytic lesions were acquired at 768×576 resolution using a Fotofinder digital dermatoscope (FotoFinder Systems Inc., 2012). 12 copies of each image were printed on $13\text{cm} \times 18\text{cm}$ photographic paper. A copy of each image and a special marker pen were given to each of 4 “junior”, 4 “senior” and 4 “expert” dermatologists (having respectively less than 1 year of experience, more than 1 year but no dermatoscopic training, more than 1 year and dermatoscopic training). Each dermatologist was then asked to independently draw with the marker the border of each lesion. The images (and borders) were scanned and realigned to the same frame of reference. Finally, the contours provided by the markers were extracted and compared. This allowed the identification, for each pixel of each original image, of the set of dermatologists classifying it as part of the lesion or of the surrounding, healthy skin.

We developed a Java implementation of our segmentation technique. In order to evaluate its efficiency on a wide range of devices, from desktops to hand-helds, we tested it on three different platforms: a Samsung Galaxy S cell phone with a 1 GHz ARM Cortex A8 processor, an ASUS Transformer Prime tablet with a 1.3 GHz Nvidia Tegra 3 processor, and a desktop PC with a 3.07 GHz Intel Core i7-950 processor. To provide a clearer evaluation of the strengths and limitations of our technique, none of our tests made use of the optional digital hair removal phase (see Subsection 3.1).

We compared our technique with three different state-of-the-art approaches, selecting a representative technique for each of the three classes introduced in Section 2. We chose techniques with publicly available implementations. For the first class, we considered the EdgeFlow algorithm (Ma and Manjunath, 2000) (<http://vision.ece.ucsb.edu/segmentation/edgeflow/software>). Recent work (Celebi et al., 2009; Silveira et al., 2009) has already shown how simple active contours methods (like GVF Snakes) perform quite poorly in terms of accuracy; we therefore chose to test a method, like EdgeFlow, which aims at detecting edges more ro-

bustly – unifying the active contour model with texture segmentation techniques. For the second class, we tested the Statistical Region Merging (SRM) algorithm (Celebi et al., 2008). For the third class, we implemented a Java version of the 2D-PCA algorithm proposed in (Silletti et al., 2009).

SRM does not work properly on lesions adjacent to the image’s borders. Thus, for its evaluation, we removed from our dataset all such images, testing it on a reduced dataset of 40 images. Our own technique produces more accurate segmentations on this reduced dataset than on the full one (see Subsection 4.2) so we effectively gave SRM an advantage by allowing it to run on an “easier” dataset.

EdgeFlow produces a set of segmented regions, but does not include a decisional step to determine which regions should be marked as part of the lesion. Again, we chose to make the comparison as biased as possible *against* our own technique, allowing EdgeFlow a perfect, instantaneous decisional step. More precisely, we assumed the decisional step would take zero time, and would choose as output for EdgeFlow the set of regions maximizing the segmentation accuracy (see Figure 5 and the following Subsection).

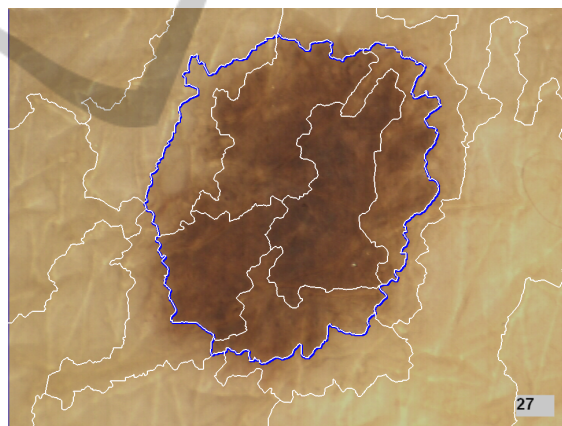


Figure 5: Melanocytic lesion segmentation using EdgeFlow. White contours identify the output of the algorithm. Blue contours identify the area considered lesional in our evaluation of EdgeFlow.

4.2 Accuracy

We measured the accuracy of a generic segmentation S by comparing it to a “ground truth” reference segmentation R , and counting the number TP of true positive pixels (classified as lesion by both segmentations), the number FP of false positive pixels (classified as lesion by S but not by R), the number FN of false negative pixels (classified as lesion by R but not by S) and the number TN of true negative pixels (classified as lesion by neither segmentation). We

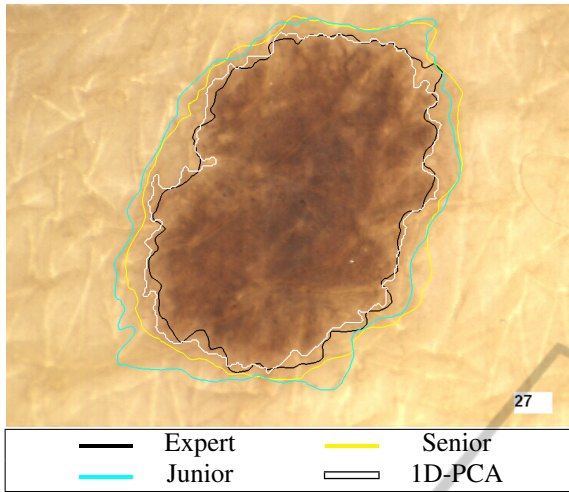


Figure 6: Melanocytic lesion segmentation performed by human dermatologists and 1D-PCA.

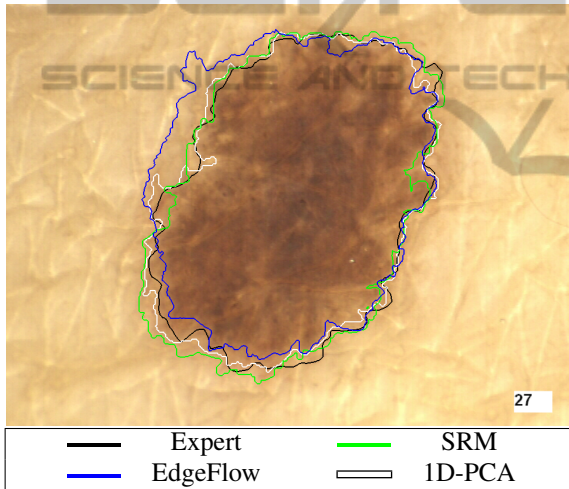


Figure 7: Melanocytic lesion segmentation performed by expert dermatologists, SRM, EdgeFlow and 1D-PCA.

then computed the *divergence of S from R* as:

$$d_s = \frac{FP + FN}{TP + FN}$$

i.e. as the ratio between the area of the misclassified region (FP+FN) and the area of the lesion itself according to the ground truth reference segmentation (TP+FN) (Hance et al., 1996).

We evaluated the different techniques by comparing their segmentations with those produced by the 4 expert dermatologists (see Table 1). 1D-PCA obtained, on average, a 12.35% divergence from expert dermatologists. In the spirit of (Silletti et al., 2009), we also evaluated the 4 senior and 4 junior dermatologists using as ground truth the segmentations produced by the 4 expert dermatologists, and each expert

Table 1: Divergence d_s (average and standard deviation) from *expert dermatologists* in the segmentation performed by different dermatologists and automated techniques. For the SRM algorithm, results refer to the reduced dataset (40 images).

Group	d_s (avg)	d_s (std)
Experts	10.40%	6.86%
Seniors	13.57%	9.54%
Juniors	17.24%	15.53%
1D-PCA	12.35%	6.98%
1D-PCA static	12.45%	7.16%
1D-PCA static w/o NR	13.44%	8.21%
2D-PCA	15.58%	7.19%
SRM	15.15%	8.65%
EdgeFlow	16.75%	8.06%

dermatologist using as ground truth the segmentations produced by the remaining 3 expert dermatologists. The average divergence of junior dermatologists from the experts, of the senior dermatologists from the experts, and of the experts from the other experts, was respectively 17.24%, 13.57% and 10.40%.

Thus, our 1D-PCA technique achieved a disagreement with expert dermatologists that was lower than that achieved by junior and senior dermatologists, and very close to the disagreement of expert dermatologists between themselves (see Figure 6). This makes it *essentially optimal* in terms of accuracy, since disagreement between experts can be viewed as an intrinsic, inevitable level of “noise” in the evaluation of melanocytic lesion border (Silletti et al., 2009).

Quite surprisingly, we observed that some simplifications applied to 1D-PCA lead to only modest reductions in accuracy. Using the simplified static 1D-PCA (Section 3.2) resulted in a negligible 0.1% loss in accuracy; eliminating the noise reduction step (see Subsection 3.3) similarly produced a very small loss in accuracy – only 1% (see Table 1). As we shall see in the following Subsection, these small accuracy losses can be traded for fairly significant speedups.

All other automated techniques exhibited worse accuracy. EdgeFlow provided the worst results, with an accuracy comparable to that of junior dermatologists, despite our “generous” evaluation which, for each image, considered lesional the set of regions minimizing divergence from the ground truth (see Subsection 4.1). The accuracy of SRM, too, was worse than that of senior dermatologists, again despite a “generous” evaluation on the easier, reduced dataset (by means of comparison, our technique improved its divergence from 12.35% to 11.87% when moving from the full dataset to the reduced one). Perhaps most surprisingly, even 2D-PCA was less accurate than 1D-PCA; this difference may be due in part to the fact that the second principal component intro-

duces more noise than information, and in part to the fact that operating on a 1D colour histogram allows one to take a slightly more sophisticated approach to the identification of the colour cluster centres and boundaries.

As a final note, we remark that our technique is also extremely robust. Many of the photographs exhibited a number of defects making segmentation harder. 1D-PCA is surprisingly resistant to minor imperfections like small air bubbles in the anti-reflective gel or shadows cast by the dermatoscope; we observed an average divergence of only 11.09% on these images (12 in total). However, images with many pixels occluded by dark hair, with large air bubbles casting deep shadows, or with incorrectly framed lesions “overflowing” from the image, lead to larger divergences (15.36% on average, on a total of 14 such images). While digital hair removal (Fiorese et al., 2011) is a solution to the first problem, the latter two clearly stress the importance of taking good photographs in the first place.

4.3 Computational Resources

Our segmentation technique is extremely fast. Segmenting any one of our test images in memory took less than 0.02 seconds on the Core i7 desktop and only 0.7 seconds on the Galaxy S cell phone (this does not account for the possible cost of preprocessing with a hair-removing tool).

Tables 2 and 3 show how the execution time can be further trimmed down by skipping some computation-intensive operations that do not significantly improve the accuracy of the segmentation.

Static 1D-PCA required 30% less execution time than 1D-PCA – while providing virtually identical accuracy. Devices with lower computational power benefit even more from this simplification: on the the Galaxy S static 1D-PCA required 45% less time than 1D-PCA. Similarly, skipping the noise reduction phase (and thus worsening accuracy by a modest 1%) reduced execution time by 30 – 40% (and by 50 – 55% in the case of static 1D-PCA). Figure 8 summarizes the computational costs of each phase.

In contrast with the (1D and 2D) PCA implementations, which are written in Java for portability, SRM and EdgeFlow are written in C (generally more efficient). Thus, we could test them only on the Core i7 platform (see Table 2). 1D-PCA outperformed both SRM and 2D-PCA by over an order of magnitude in terms of running time; and EdgeFlow by several orders of magnitude (even though we “charged” EdgeFlow no time costs for the choice of the lesional region set – see Subsection 4.1).

Table 2: Execution time in milliseconds of 1D-PCA, static 1D-PCA with and without noise reduction, 2D-PCA, SRM and EdgeFlow on a desktop PC mounting an Intel Core i7-950 processor.

	Core i7
1D-PCA	17
1D-PCA static	12
1D-PCA static w/o NR	7
2D-PCA	199
SRM	189
EdgeFlow	104789

Table 3: Execution time in milliseconds of 1D-PCA, static 1D-PCA with noise reduction disabled or enabled and 2D-PCA on a Samsung Galaxy S cell phone and on an ASUS Transformer Prime tablet.

	Galaxy	Transformer
1D-PCA	733	411
1D-PCA static	407	286
1D-PCA static w/o NR	185	120
2D-PCA	5986	2778

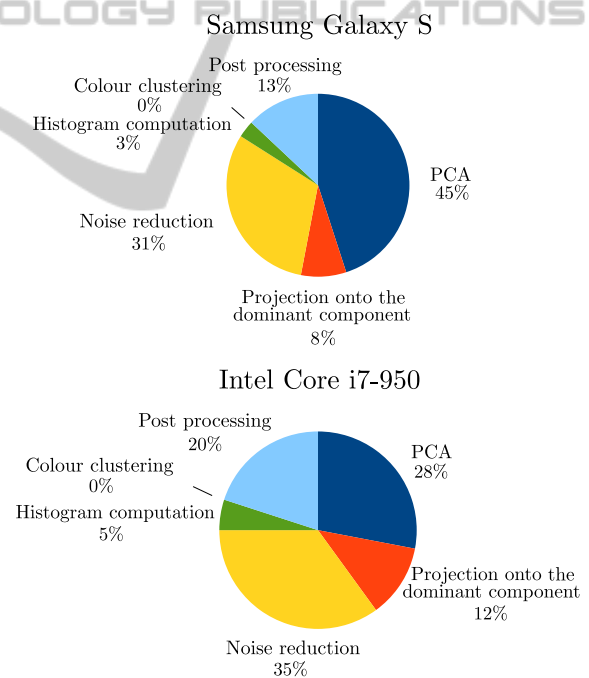


Figure 8: Time cost breakdown of our technique on a Samsung Galaxy S cell phone and on a desktop PC mounting an Intel Core i7-950 processor.

The main reason for the extreme computational performance of 1D-PCA is the fact that the 1D colour histogram can be processed extremely quickly: only a handful of simple operations are required for each of its 256 points, without any need of costly iterations. And since PCA, colour histogram creation, and morphological postprocessing all boil down to “stream-

ing” the image while performing a few simple operations on each of its pixels, the total cost of segmenting the image is essentially that of scanning it a few times.

5 CONCLUSIONS

Our simple technique for melanocytic lesion segmentation is *extremely* fast. A Java implementation of it can segment a large dermatoscopic image in the time required to simply scan the image a handful of times – a fraction of a second even on hand-held devices with modest computational resources. This represents an improvement of an order of magnitude or more over state-of-the-art techniques.

At the same time, our technique does not sacrifice accuracy. It appears more accurate than state-of-the-art techniques. Perhaps more importantly, it appears almost as accurate as *any* segmentation technique can be, since expert dermatologists disagree with it only slightly more than they disagree between themselves – and less than they disagree with dermatologists of little, or even moderate, experience.

Finally, our technique is extremely robust. It does not require careful hand-tuning; a single parameter controls how “tight” the segmentation is. It tolerates very well small photographic defects, such as small air bubbles or uneven lighting. It is only slightly less robust in the face of hair (which could be easily removed, physically or through digital preprocessing), larger air bubbles, or improper lesion framing. In fact, our technique is so robust that one can achieve almost as accurate results with a crude simplification of it which, instead of projecting the colour space of each image onto its principal component, projects it onto a precomputed space independent of the image – allowing even faster processing, as well as use of (cheaper) monochromatic image acquisition equipment.

ACKNOWLEDGEMENTS

This work was supported by Univ. Padova under strategic project AACSE. F. Peruch, F. Bogo, M. Bressan and V. Cappelleri were supported in part by fellowships from Univ. Padova. The authors would thank the Dermatology Unit of Univ. Padova for its invaluable help.

REFERENCES

Abdi, H. and Williams, L. J. (2010). Principal component analysis. *WIREs Comp. Stat.*, 2(4).

- Belloni Fortina, A., Peserico, E., Silletti, A., and Zattra, E. (2011). Where’s the naevus? Inter-operator variability in the localization of melanocytic lesion border. *Skin Res. and Tech.*, 18(3).
- Celebi, M. E., Aslandogan, Y., and Van Stoecker, W. (2007). Unsupervised border detection in dermoscopy images. *Skin Res. and Tech.*, 13(4).
- Celebi, M. E., Iyatomi, H., Schaefer, G., and Stoecker, W. V. (2009). Lesion border detection in dermoscopy images. *Comput. Med. Imaging Graph.*, 33(2).
- Celebi, M. E., Kingravi, H. A., Iyatomi, H., Aslandogan, Y. A., Van Stoecker, W., Moss, R. H., Malters, J. M., Grichnik, J. M., Marghoob, A. A., Rabinovitz, H. S., and Menzies, S. W. (2008). Border detection in dermoscopy images using statistical region merging. *Skin Res. and Tech.*, 14(3).
- Chang, F., Chen, C.-J., and Lu, C.-J. (2004). A linear-time component-labeling algorithm using contour tracing technique. *Comput. Vis. Image Underst.*, 93(2).
- Cucchiara, R., Grana, C., Seidenari, S., and Pellacani, G. (2002). Exploiting color and topological features for region segmentation with recursive fuzzy c-means. *Machine Graph. and Vision*, 11(2/3).
- Erkol, B., Moss, R. H., Stanley, R. J., Van Stoecker, W., and Hvatum, E. (2005). Automatic lesion boundary detection in dermoscopy images using gradient vector flow snakes. *Skin Res. and Tech.*, 11(1).
- Fiorese, M., Peserico, E., and Silletti, A. (2011). Virtual-Shave: Automated hair removal from digital dermatoscopic images. In *Proc. of IEEE EMBC*.
- FotoFinder Systems Inc. (2012). Fotofinder dermoscope. <http://www.fotofinder.de/en.html>.
- Gao, J., Zhang, J., Fleming, M. G., Pollak, I., and Cognetta, A. B. (1998). Segmentation of dermatoscopic images by stabilized inverse diffusion equations. In *Proc. of ICIP*.
- Hance, G. A., Umbaugh, S. E., Moss, R. H., and Stoecker, W. V. (1996). Unsupervised color image segmentation with application to skin tumor borders. In *Proc. of IEEE EMBC*.
- Joel, G., Schmid-Saugeon, P., Guggisberg, D., Cerottini, J. P., Braun, R., Krischer, J., Saurat, J. H., and Murat, K. (2002). Validation of segmentation techniques for digital dermoscopy. *Skin Res. and Tech.*, 8(4).
- Ma, W.-Y. and Manjunath, B. S. (2000). EdgeFlow: a technique for boundary detection and image segmentation. *IEEE Trans. on Image Processing*, 9(8).
- Martin-Herrero, J. (2007). Hybrid object labelling in digital images. *Machine Vision and Applications*, 18(1).
- Melli, R., Grana, C., and Cucchiara, R. (2006). Comparison of color clustering algorithms for segmentation of dermatological images. In *Proc. of SPIE*.
- Park, J.-M., Looney, C. G., and Chen, H.-C. (2000). Fast connected component labeling algorithm using a divide and conquer technique. In *Proc. of ISCA 15th Conference on Computers and Their Applications*.
- Rigel, D. S., Friedman, R. J., and Kopf, A. W. (1996). The incidence of malignant melanoma in the United States: issues as we approach the 21st century. *JAAD*, 34(5, Part 1).

- Schmid, P. (1999). Segmentation of digitized dermatoscopic images by two-dimensional color clustering comparison. *IEEE Trans. on Medical Imaging*, 18(2).
- Silletti, A., Peserico, E., Mantovan, A., Zattra, E., Peserico, A., and Belloni Fortina, A. (2009). Variability in human and automatic segmentation of melanocytic lesions. In *Proc. of IEEE EMBC*.
- Silveira, M., Nascimento, J., Marques, J., Marcal, A., Mendonca, T., Yamauchi, S., Maeda, J., and Rozeira, J. (2009). Comparison of segmentation methods for melanoma diagnosis in dermoscopy images. *Selected Topics in Signal Processing*, 3(1).
- Stolz, W., Merkie, T., Cagnetta, A., Vogt, T., Landthaler, M., Bilek, P., and Plewig, G. (1994). The ABCD rule of dermatoscopy. *JAAD*, 30(4).
- Suzuki, K., Horiba, I., and Sugie, N. (2003). Linear-time connected-component labeling based on sequential local operations. *Comput. Vis. Image Underst.*, 89(1).
- Szeliski, R. (2010). *Computer vision: algorithms and applications*. Springer.
- Wang, H., Chen, X., Moss, R. H., Stanley, R. J., Stoecker, W. V., Celebi, M. E., Szalapski, T. M., Malters, J. M., Grichnik, J. M., Marghoob, A. A., Rabinovits, H. S., and Menzies, S. W. (2010). Watershed segmentation of dermoscopy images using a watershed technique. *Skin Res. and Tech.*, 16(3).